Benchmarked computation of time-domain viscoelastic Love numbers for adiabatic mantles

S.B. Kachuck [1,]* and L.M. Cathles, III[2]

[1]*Department of Physics, Cornell University, Ithaca, NY, USA. E-mail: sbk83@cornell.edu*
[2]*Earth and Atmospheric Sciences, Cornell University, Ithaca, NY, USA*

SUMMARY

The viscoelastic load Love numbers encapsulate the Earth's rheology in a remarkably efficient fashion. When multiplied by a sudden increment of spherical harmonic load change, they give the horizontal and vertical surface displacements and gravity change at all later times. Incremental glacial load changes thus need only be harmonically decomposed, multiplied by the Love numbers and summed to predict the Earth's response to glacial load redistributions. The computation of viscoelastic Love numbers from the elastic, viscous and adiabatic profiles of the Earth is thus the foundation upon which many glacial isostatic adjustment models are based. Usually, viscoelastic Love numbers are computed using the Laplace transform method, employing the correspondence principle to convert the viscoelastic equations of motion into the elastic equations with complex material parameters. This method works well for a fully non-adiabatic Earth, but can accommodate realistic partially adiabatic and fully adiabatic conditions only by changing the Earth's density profile. An alternative method of Love number computation developed by Cathles (1975) avoids this dilemma by separating the elastic and viscous equations of motion. The separation neglects a small solid-elastic/fluid-elastic transition for compressible deformation, but allows freely defining adiabatic, partially adiabatic or fully non-adiabatic profiles in the mantle without changing the Earth's density profile. Here, we update and fully describe this method and show that it produces Love numbers closely similar to those computed for fully non-adiabatic earth models computed by the correspondence principle, finite element and other methods. The time-domain method produces Love numbers as good as those produced by other methods and can also realistically accommodate any degree of mantle adiabaticity. All method implementations are available open source.

Key words: Phase transitions; Loading of the Earth; Numerical solutions; Dynamics of lithosphere and mantle; Rheology: crust and lithosphere; Rheology: mantle.

1 INTRODUCTION

Numerical models of the mantle's self-gravitating, viscoelastic deformation in response to shifting surface loads are used to predict local sea level changes, correct observations of geodetic measurements and constrain mantle rheology and glacial chronologies (Steffen & Wu 2011; Peltier *et al.* 2015). For model Earth's mantles in which material parameters vary more with depth than lateral location, radial symmetry can be assumed and the spherical harmonic transformations employed. Solving the equations of motion and gravity gives depth-dependent displacements, stresses and perturbations to gravity in response to the application of a spherical–harmonic load. When normalized to the load's gravitational potential, the computed surface displacements and gravitational potential are called the loading Love numbers (Peltier 1974; Wu & Peltier 1982; Vermeersen *et al.* 1996b). Methods differ in how they perform the integration through the mantle and, more importantly, how they treat the time dependence of the response.

---

* Now at: Climate and Space Sciences and Engineering, University of Michigan, Ann Arbor, MI, USA.

The most commonly used technique today for computing the time-dependent viscoelastic Love numbers is to transform the time variable t into the complex frequency s using the Laplace transform. In the Laplace domain, the viscoelastic equation of state for a Maxwell viscoelastic body has the form of the elastic equations of motion with the elastic parameters replaced with s-dependent expressions that incorporate the viscosity of the material. The time-dependent Love numbers are found when the s-dependent Love numbers are inverted back to the time domain. That the elastic equation of motion can be used to determine the viscoelastic solution by making the elastic parameters complex is called the correspondence principle (Cathles 1975; Wu & Peltier 1982; Sabadini *et al.* 2016). Multiple implementations of the correspondence principle method of Love number computation were shown to agree with each other and with finite element methods for the self-gravitating, incompressible deformation of layered mantles in the benchmarking exercise of Spada *et al.* (2011).

In the correspondence principle methods, the mantle is typically stratified into layers within which the material properties are constant. In this case, the inverse Laplace transformation is dominated by isolated, first-order poles in the complex plane, called the viscoelastic normal modes (Peltier 1985; Wolf 1985). Each mode can be associated with aspects of the mantle model considered (Wolf 1985). For instance, there are modes associated with the relaxation of buoyancy forces at the lithosphere and from the density contrast between the mantle and the core (called L0 and C0, respectively). There are two modes associated with each jump in viscoelastic parameters at each layer boundary, called the transient modes (Ts). These adjust quickly and have small amplitudes. Finally, there are modes associated with jumps in density at the layer boundaries, called the mantle modes (Ms). These adjust more slowly, are larger in magnitude and have more impact on the computed viscoelastic deformation. All the density jumps inhibit flow because buoyancy forces build that slow their displacement. They must, therefore, be considered either compositional discontinuities or the boundaries of a fully non-adiabatic phase change (Wu & Peltier 1982; Sabadini *et al.* 2016).

This last statement has important implications. In an adiabatic fluid, a displaced parcel of material enclosed in an insulating but deformable sack immediately conforms to its new environment (in density, temperature, etc.). Flow mimics this adiabatic sack, and so moves in an adiabatic mantle as if any changes in density were not present (Turner 1979). Only the non-adiabatic portion of density gradients in the mantle inhibit flow. The density discontinuities bounding the layers of a correspondence principle solution are fully non-adiabatic and introduce a buoyant mode that affects the timing of total viscoelastic deformation (Nakada 1999; Wolf & Kaufmann 2000). Not all the density changes in the Earth's mantle are non-adiabatic, however. At least half the approximately 2000 kg m^{-3} increase in density between the top and bottom of the mantle is due to self-compression and hence is adiabatic (Dziewonski & Anderson 1981; Johnston *et al.* 1997). Furthermore, a density jump at a phase boundary could be adiabatic if heat is being advected through it by mantle flow quickly enough that an adiabatic temperature profile is maintained across it (Cathles 1975; Johnston *et al.* 1997). Deciding which parts of the changes of density in the mantle are adiabatic and which are not is not a straight-forward task, and, therefore, a method that allows the fraction of a density change that is non-adiabatic to be freely specified is useful.

Separating self-compression from non-adiabatic density changes within the correspondence principle method has been addressed by Nakada (1999) and Cambiotti & Sabadini (2010). They separated the density stratification into the density change expected from elastic self-compression and a remaining 'compositional' (by which they mean non-adiabatic) component. As described by Cambiotti & Sabadini (2010), this results in a set of modes (the C modes) that are associated with non-adiabatic stratification. They simulate an adiabatic or partially adiabatic mantle by reducing the magnitude of the compositional component. This changes the mass of the Earth and sacrifices accuracy in the gravitational perturbations (Fjeldskaar & Cathles 1984).

Challenges also arise within the correspondence principle method when considering mantles that are compressible or have parameters that vary continuously with depth because non-isolated poles (Fang & Hager 1995; Han & Wahr 1995) or poles off the real axis (Al-Attar 2011) appear that are difficult to locate and integrate. Methods have been developed to approximate the poles (Vermeersen *et al.* 1996b), and to handle them by carrying out a more comprehensive inverse transform integration (Klemann *et al.* 2003; Tanaka *et al.* 2006), but appropriately modelling compressibility may require addressing additional issues associated with continuous parameters (Wolf 1991; Wolf & Kaufmann 2000).

Another method for computing the time-dependent viscoelastic Love numbers, avoids these problems of compressibility, continuously varying parameters and artificial sources of buoyancy (e.g. phase boundaries that may be adiabatic), is to compute the elastic and viscous deformations separately at each time step of the evolution and add them together. This time-domain method was developed by Cathles (1975). The advantage of separating the elastic and viscous equations of motion is that it allows an explicit distinction to be made between adiabatic and non-adiabatic density gradients without modifying the total densities that are the source of the gravity field. Hanyk *et al.* (1996) also presents a time-domain method. Although it does not discard the solid-elastic/fluid-elastic transition, it also cannot include a separate non-adiabatic density parameter and so will encounter the same difficulties when treating partially non-adiabatic conditions as described for the correspondence principle next.

As discussed extensively in Cathles (1975), linearly separating the viscous and elastic equations requires neglecting the small elastic change associated with the transition from the initial solid-elastic response to loading and the ultimate fluid-elastic response. As first noted by Cathles (1971), the initial response of a viscoelastic body to harmonic loading is purely elastic, but after a period on the order of the Maxwell time (the ratio of the viscosity to the elastic rigidity or $\sim$300 yr for a mantle with 10^{21} Pa s viscosity and 10^{11} Pa rigidity) the dilational elastic response relaxes. The increase in elastic displacements during this solid-elastic/fluid-elastic transition (elsewhere called the elasticoviscous transition; e.g. Peltier 1974) is less than 6 per cent of the initial elastic response for all wavelength loads, and

is thus quite negligible. As this transition is between elastic shear and compressive displacements, it does not occur in incompressible materials.

The early work by Cathles (1975) was not cast in terms of Love numbers and did not include the elastic deformation of the lithosphere. This paper fully describes the Cathles (1975) method in modern terms and incorporates the elastic deformation of the crust. We benchmark the resulting time-domain Love numbers against Love numbers computed using the correspondence principle and discuss the small differences between the two methods. Our purpose here is not to model the viscoelastic response of the Earth to glacial load changes. It is simply to compare two different methods of computing the Love numbers that are used to compute these changes. The clear and complete benchmarking offered here should be useful to those interested in using this method, available in the open-source package `giapy`[1] [Glacial Isostatic Adjustment (GIA) in PYthon].

The benchmarking exercises reported here compare the viscoelastic Love numbers computed using our time-domain method to the viscoelastic Love numbers published in tests 5/1 and 6/1 of Spada *et al.* (2011). Since Spada *et al.* (2011) found close agreement between the Love numbers computed using many different theoretical and computational methods in both of these benchmark tests, including the correspondence principle (Spada 2003; Spada & Boschi 2006) and finite element methods (Martinec 2000), the comparison applies to a broad set of computations by many workers using a variety methods. We show next that our elastic Love numbers are identical to those computed by other methods. There are slight differences in the viscoelastic Love numbers, but they do not produce significant differences in isostatic adjustment when used to calculate the response to the instantaneous loading of a spherical ice dome. We show that our method can reproduce the adiabatic and non-adiabatic Love numbers as computed by Nakada (1999) without changing the Earth's density gradient. Compressible elastic Love numbers computed by us for PREM (Dziewonski & Anderson 1981) agree with those computed by Pan *et al.* (2015), and the compressibility we calculate affects viscoelastic deformation in the same way as shown for the correspondence principle methods by Vermeersen *et al.* (1996b) and Sabadini *et al.* (2016).

In what follows, we first fully describe the time-domain method, emphasizing how non-adiabatic sources of buoyancy within the mantle are treated and giving full details and deriving the equations in supplemental material. We also describe our transformed relaxation implementation for the spatial integration through the mantle. We then show that the time-domain solution of the decoupled viscous and elastic equations generates viscoelastic Love numbers similar to those computed using the correspondence principle. Finally, we discuss the minor differences noted in this comparison. All of the methods described here are available as part of the open-source giapy (GIA in PYthon) package, which also includes a benchmarked implementation of the sea level equation (Martinec *et al.* 2018).

2 THEORY

2.1 Self-gravitating elasticity

The self-gravitating, compressible elastic equations of motion linearized for small perturbative displacements **u** are given by the following constitutive, momentum and gravitational potential equations (Cathles 1975; Peltier 1982; Tromp & Mitrovica 1999):

$$\tau = \lambda \mathrm{Tr}(\varepsilon)\mathbf{I} + 2\mu\varepsilon, \tag{1}$$

$$0 = (\nabla \cdot \tau)\mathbf{I} - \nabla(\rho g \mathbf{u} \cdot \hat{\mathbf{r}}) + g\nabla \cdot (\rho\mathbf{u})\hat{\mathbf{r}} - \rho\nabla\psi, \tag{2}$$

$$\nabla^2 \psi = -4\pi G \nabla \cdot (\rho\mathbf{u}), \tag{3}$$

where τ is the stress tensor, $\varepsilon = \frac{1}{2}(\nabla\mathbf{u} + \nabla\mathbf{u}^T)$ is the strain tensor, ψ is the perturbation to the gravitational potential, **I** is the identity tensor and G is Newton's gravitational constant ($6.6732 \times 10^{-11}\,\mathrm{N\,m^2\,kg^{-2}}$). We assume that the material parameters $\lambda(r)$, $\mu(r)$, $\rho(r)$ and $g(r)$ (the first and second Lamé parameters, the unperturbed density and gravity, respectively) are all functions of the radius r alone, specified by a globally averaged model, for example, PREM (Dziewonski & Anderson 1981).

So that the system includes only first-order derivatives, we introduce a new variable, q, that we define as the first radial derivative of the perturbation to the gravitational potential $q \equiv \partial\psi/\partial r$, or the perturbation to the radial acceleration due to gravity. This definition of q is different from the generalized gravitational flux frequently used in the literature (Farrell 1972; pg 772), but retains explicit dependence of the equations of motion on the density gradient. This is important when separating the adiabatic and non-adiabatic density gradients as discussed next. See also the discussion surrounding eqs (A.27) and (A.28) in the Supporting Information text A.

Following the notation of Pan *et al.* (2015), each variable is expanded into its vector or scalar spherical harmonic fields:

$$\mathbf{u}(\mathbf{r}) = \sum_{\ell,m} [U_L(r)\mathbf{L}(\theta, \phi) + U_M(r)\mathbf{M}(\theta, \phi) + U_N(r)\mathbf{N}(\theta, \phi)], \tag{4}$$

[1]https://github.com/skachuck/giapy

$$\tau_{,r}(\mathbf{r}) = \sum_{\ell,m} [T_L(r)\mathbf{L}(\theta, \phi) + T_M(r)\mathbf{M}(\theta, \phi) + T_N(r)\mathbf{N}(\theta, \phi)], \tag{5}$$

$$\psi(\mathbf{r}) = \sum_{\ell,m} \Psi(r)Y_\ell^m(\theta, \phi), \tag{6}$$

$$q(\mathbf{r}) = \sum_{\ell,m} Q(r)Y_\ell^m(\theta, \phi). \tag{7}$$

$Y_\ell^m(\theta, \phi)$ is the spherical harmonic function of order ℓ and rank m. The subscript L identifies coefficients for radial vectors $\mathbf{L}(\theta, \phi) = Y_\ell^m(\theta, \phi)\hat{\mathbf{r}}$. Similarly, subscripts M and N identify poloidal and toroidal coefficients, associated with basis vectors $\mathbf{M}(\theta, \phi) = \nabla Y_\ell^m(\theta, \phi)$ and $\mathbf{N}(\theta, \phi) = \hat{\mathbf{r}} \times \nabla Y_\ell^m(\theta, \phi)$.

The elastic equations of motion (1 and 2) are then expressed

$$\frac{\partial}{\partial r} \begin{bmatrix} U_L^E \\ U_M^E \\ T_L \\ T_M \\ \Psi \\ Q \end{bmatrix} = \mathbf{A}^E \begin{bmatrix} U_L^E \\ U_M^E \\ T_L \\ T_M \\ \Psi \\ Q \end{bmatrix} + \mathbf{b}^E, \tag{8}$$

with

$$\mathbf{A}^E = \begin{bmatrix} -\dfrac{2\lambda}{r(\lambda + 2\mu)} & \dfrac{\ell(\ell+1)\lambda}{r(\lambda + 2\mu)} & \dfrac{1}{\lambda + 2\mu} & 0 & 0 & 0 \\ -\dfrac{1}{r} & \dfrac{1}{r} & 0 & \dfrac{1}{\mu} & 0 & 0 \\ \left(\dfrac{4\mu(3\lambda+2\mu)}{r^2(\lambda+2\mu)} - \dfrac{2g\rho}{r} + 4\pi G\rho^2\right) & -\left(\dfrac{2\mu(3\lambda+2\mu)}{r^2(\lambda+2\mu)} - \dfrac{g\rho}{r}\right)\ell(\ell+1) & -\dfrac{4\mu}{r(\lambda+2\mu)} & \dfrac{\ell(\ell+1)}{r} & 0 & \rho \\ \left(\dfrac{\rho g}{r} - \dfrac{2\mu(3\lambda+2\mu)}{r^2(\lambda+2\mu)}\right) & \dfrac{2\mu(2(\lambda+\mu)\ell(\ell+1) - (\lambda+2\mu))}{r^2(\lambda+2\mu)} & -\dfrac{\lambda}{r(\lambda+2\mu)} & -\dfrac{3}{r} & \dfrac{\rho}{r} & 0 \\ 0 & 0 & 0 & 0 & 0 & 1 \\ -4\pi G\left(\rho' + \dfrac{4\mu\rho}{r(\lambda+2\mu)}\right) & 8\pi G\dfrac{\ell(\ell+1)\mu\rho}{r(\lambda+2\mu)} & -4\pi G\dfrac{\rho}{\lambda+2\mu} & 0 & \dfrac{\ell(\ell+1)}{r^2} & -\dfrac{2}{r} \end{bmatrix}, \tag{9}$$

in which ρ' is the density gradient with respect to radius ($\partial\rho/\partial r$) and the superscript E indicates an elastic component. This is identical to the matrix A given by eqs 9(a–f) in Wu & Peltier (1982), with the important exception of terms in the last two rows, which are different as a result of the choice of the definition of the gravitational flux, q. This choice is made so that there is an explicit dependence of the gravity perturbation on the density gradient ρ'. This allows us to separate the density gradient into a non-adiabatic component ρ'_{nonad} (which affects viscous flow due to a buoyancy term introduced next) and an adiabatic component ρ'_{ad} (which does not)

$$\rho' = \rho'_{\text{nonad}} + \rho'_{\text{ad}}, \tag{10}$$

while leaving the total density gradient (which affects the elastic and gravitational perturbations) unchanged. Density gradients associated with self-compression are adiabatic and should be incorporated in the ρ'_{ad} term. The inhomogeneous vector $\mathbf{b}^E$ incorporates the stresses and gravitational effects associated with viscous displacement of non-adiabatic density gradients, and is defined in eq. (28) below.

A full derivation of this matrix may be found in Supporting Information text A. The toroidal components (subscript N) are independent of the radial and poloidal components. As no toroidal stresses are present in mantles with spherically symmetric material parameters loaded at their surface, these deformations are exactly zero and not considered here.

It is common to normalize the displacements and perturbed gravity potential at the surface of the Earth in response to an applied surface load σ (e.g. Wu & Peltier 1982; eq. 12). When normalized to the gravitational potential of the applied load, these surface perturbations are called Love numbers. The Love numbers are defined as

$$\begin{bmatrix} h \\ l \\ k_d \end{bmatrix} = \frac{1}{\Psi_l} \begin{bmatrix} g_0 U_L \\ g_0 U_M \\ \Psi_d \end{bmatrix}_{r_E}, \tag{11}$$

where g_0 is the acceleration due to gravity at the Earth's surface. The gravitational potential of the load is

$$\Psi_l = \frac{4\pi G r_E}{2\ell + 1} C_\ell^m, \tag{12}$$

where C_ℓ^m are the expansion coefficients of the surface load $\sigma(\theta, \phi) = \sum_{\ell, m} C_\ell^m Y_\ell^m(\theta, \phi)$. Here, k_d and Ψ_d refer to the perturbations of the gravitational potential due to the deformation alone, excluding the effect of the load. Including the self-gravitation of the load gives us $k = k_d + 1$. Normalization makes it easier to evaluate the significance of terms in the equations of motion and reduces numerical errors.

It is convenient to consider azimuthally symmetric, unit loads so that all $C_\ell^0 \equiv 1 \, \mathrm{kg/m^{-2}}$. The response to an arbitrary load can then be found by decomposing the load into spherical harmonic coefficients, multiplying each coefficient by its order's Love number and synthesizing back into the spatial domain.

To keep all terms of order unity in the equations of motion in eq. (8), we define $L = \ell l$ and $K = \ell k$. Normalization for the remaining variables (T_L, T_M, Q) is based on the surface boundary conditions, giving

$$h = \frac{(2\ell + 1)g_0}{4\pi Gr_E C_\ell^m} U_L; \qquad L = \frac{\ell(2\ell + 1)g_0}{4\pi Gr_E C_\ell^m} U_M; \qquad k_d = \frac{2\ell + 1}{4\pi Gr_E C_\ell^m} \Psi_d; \tag{13}$$

$$f_L = \frac{1}{g_0 C_\ell^m} T_L; \qquad F_M = \frac{\ell}{g_0 C_\ell^m} T_M; \qquad q = \frac{1}{4\pi G C_\ell^m} Q. $$

Units are removed from parameters using the following scales:

$$\tilde{r} = r/r_E; \qquad \tilde{g} = g/g_0; \qquad \tilde{\rho} = \rho/\bar{\rho} \equiv \rho / \frac{g_0}{4\pi Gr_E}; \qquad \tilde{\lambda}, \tilde{\mu} = \lambda, \mu/\bar{\rho} g_0 r_E. \tag{14}$$

With these choices, which differ from some of the literature (e.g. Vermeersen *et al.* 1996b), all normalized parameters are of unit magnitude.

The normalized surface boundary conditions for a load with no horizontal tractions are

$$\begin{bmatrix} f_L \\ F_M \\ q \end{bmatrix}_{r = r_E} = \begin{bmatrix} -1 \\ 0 \\ -1 - \dfrac{1}{2\ell + 1} \left(\tilde{\rho} h^E + (1 + \ell) k_d \right) \end{bmatrix}_{r = r_E}. \tag{15}$$

The bottom boundary conditions are the stresses and gravitational perturbations from the displacement of the boundary between the mantle and the inviscid core:

$$\begin{bmatrix} f_L \\ F_M \\ q \end{bmatrix}_{r = r_c} = \frac{1}{2\ell + 1} \begin{bmatrix} \tilde{\rho}_c \tilde{g}_c h^E + \tilde{\rho}_c k_d \\ 0 \\ (\tilde{\rho}_c - \tilde{\rho}_m) h^E + \dfrac{\ell}{\tilde{r}_c} k_d \end{bmatrix}_{r = r_c}, \tag{16}$$

where ρ_c and ρ_m are the densities of the core and mantle on either side of the core mantle boundary. These are the same boundary conditions given elsewhere (Cathles 1975; Sabadini *et al.* 1982; Wu & Peltier 1982; Vermeersen *et al.* 1996b), re-expressed in terms of the unknown quantities of interest to facilitate our method of computation, as described below.

Finally, we introduce a novel transformation of the radial variable that simplifies the equations and their solution. For a flat half-space, the deformations and stresses decay into the bulk exponentially with a length-scale proportional to the wavelength of the load (Cathles 1975) so that smaller loads deform ever shallower regions of the mantle (Wu & Peltier 1982). This suggests we rescale the radial vector as

$$\chi \equiv e^{-\frac{(2\ell + 1)}{2}(1 - \tilde{r})}, \tag{17}$$

so that an equispaced mesh in χ samples regions of the mantle where the solutions actually change (i.e. closer to the surface for higher ℓ). Normalized, and in the transformed variable, the system in eq. (9) is

$$\frac{\partial}{\partial \chi} \begin{bmatrix} h^E \\ L^E \\ f_L \\ F_M \\ k_d \\ q \end{bmatrix} = \hat{\mathbf{A}}^E \cdot \begin{bmatrix} h^E \\ L^E \\ f_L \\ F_M \\ k_d \\ q \end{bmatrix} + \mathfrak{b}^E \tag{18}$$

with

$$
\mathbf{A}^E = \frac{1}{\chi}
\begin{bmatrix}
-\dfrac{4\tilde{\lambda}}{\tilde{r}(\tilde{\lambda}+2\tilde{\mu})}\dfrac{1}{2\ell+1} & \dfrac{\tilde{\lambda}}{\tilde{r}(\tilde{\lambda}+2\tilde{\mu})}\dfrac{2(\ell+1)}{2\ell+1} & \dfrac{2}{\tilde{\lambda}+2\tilde{\mu}} & 0 & 0 & 0 \\[2mm]
-\dfrac{1}{\tilde{r}}\dfrac{2\ell}{2\ell+1} & \dfrac{1}{\tilde{r}}\dfrac{2}{2\ell+1} & 0 & \dfrac{2}{\tilde{\mu}} & 0 & 0 \\[2mm]
\left(\dfrac{4\tilde{\mu}(3\tilde{\lambda}+2\tilde{\mu})}{\tilde{r}^2(\tilde{\lambda}+2\tilde{\mu})}-\dfrac{4\tilde{\rho}\tilde{g}}{\tilde{r}}\right)\dfrac{2}{(2\ell+1)^2} & -\left(\dfrac{2\tilde{\mu}(3\tilde{\lambda}+2\tilde{\mu})}{\tilde{r}^2(\tilde{\lambda}+2\tilde{\mu})}-\dfrac{\tilde{\rho}\tilde{g}}{\tilde{r}}\right)\dfrac{2(\ell+1)}{(2\ell+1)^2} & -\dfrac{4\tilde{\mu}}{\tilde{r}(\tilde{\lambda}+2\tilde{\mu})}\dfrac{2}{2\ell+1} & \dfrac{1}{\tilde{r}}\dfrac{2(\ell+1)}{2\ell+1} & -\dfrac{\tilde{\rho}}{\tilde{r}}\dfrac{2(\ell+1)}{(2\ell+1)^2} & \dfrac{2\tilde{\rho}}{2\ell+1} \\[2mm]
\left(\dfrac{\tilde{\rho}\tilde{g}}{\tilde{r}}-\dfrac{2\tilde{\mu}(3\tilde{\lambda}+2\tilde{\mu})}{\tilde{g}\tilde{r}^2(\tilde{\lambda}+2\tilde{\mu})}\right)\dfrac{2\ell}{(2\ell+1)^2} & \dfrac{4\tilde{\mu}(2(\tilde{\lambda}+\tilde{\mu})\ell(\ell+1)-(\tilde{\lambda}+2\tilde{\mu}))}{\tilde{r}^2(\tilde{\lambda}+2\tilde{\mu})(2\ell+1)^2} & -\dfrac{\tilde{\lambda}}{\tilde{r}(\tilde{\lambda}+2\tilde{\mu})}\dfrac{2\ell}{2\ell+1} & -\dfrac{3}{\tilde{r}}\dfrac{2}{2\ell+1} & \dfrac{\tilde{\rho}}{\tilde{r}}\dfrac{2\ell}{(2\ell+1)^2} & 0 \\[2mm]
0 & 0 & 0 & 0 & 0 & 2 \\[2mm]
-\left(\tilde{\rho}'+\dfrac{4\tilde{\mu}\tilde{\rho}}{\tilde{r}(\tilde{\lambda}+2\tilde{\mu})}\right)\dfrac{2}{(2\ell+1)^2} & \dfrac{2\tilde{\mu}\tilde{\rho}}{\tilde{r}(\tilde{\lambda}+2\tilde{\mu})}\dfrac{2(\ell+1)}{(2\ell+1)^2} & -\dfrac{\tilde{\rho}}{\tilde{\lambda}+2\tilde{\mu}}\dfrac{2}{2\ell+1} & 0 & \dfrac{2\ell(\ell+1)}{\tilde{r}^2(2\ell+1)^2} & -\dfrac{4}{\tilde{r}(2\ell+1)}
\end{bmatrix}, \quad (19)
$$

with material parameters linearly interpolated to the χ mesh locations. There are now no terms with an ℓ in the numerator that is unmatched by an ℓ in the denominator, so no terms diverge in the limit of small loads ($\ell \to \infty$). For large ℓ, this matrix simplifies to a form where small wavelength perturbations to the Earth's internal gravity do not contribute to the dynamics (see Supporting Information text B).

We solve eq. (18) using the relaxation method of Press (2007; section 18.3). In this method, the differential equations are replaced explicitly with finite difference equations in the variable χ and a test solution is iteratively refined by backpropagation from one boundary to another until the average error in the finite differences between points in the solution mesh are within a desired tolerance (10^{-14}). The method takes advantage of the slow variation of the normalized solutions with respect to order number and time (frequency). Using the previous order number's or time step's (frequency's) solution as the initial guess, the method usually requires only one iteration to converge.

2.2 Viscoelasticity

For a fluid with dynamic viscosity η, the constitutive equation that relates stresses τ to shear rate $\dot{\varepsilon}$ is given as

$$\tau = 2\eta\dot{\varepsilon}, \tag{20}$$

where the dot over a function represents a derivative with respect to time. In a Maxwell fluid, each material element is modelled as a viscous and elastic element in parallel, with equal stresses and displacements that add. The constitutive equation for the Maxwell body can be expressed (Cathles 1975; Wu & Peltier 1982) as

$$\dot{\tau} + \frac{\mu}{\eta}\left(\tau - \frac{1}{3}\mathrm{Tr}(\tau)\mathbf{I}\right) = \lambda\,\mathrm{Tr}(\dot{\varepsilon})\mathbf{I} + 2\mu\dot{\varepsilon}. \tag{21}$$

Our approach to the time dependence is to linearly separate the elastic and viscous displacements, allowing them to influence each other via stresses and gravity, as in Cathles (1975). In this view, the total viscoelastic displacements are expressed as the sum of the elastic and viscous displacements, computed at each time:

$$h^{\mathrm{VE}}(t) = h^E(t) + \int_{-\infty}^{t} \dot{h}^V(t')\mathrm{d}t', \tag{22}$$

$$L^{\mathrm{VE}}(t) = L^E(t) + \int_{-\infty}^{t} \dot{L}^V(t')\mathrm{d}t'. \tag{23}$$

This is similar to the model of Hanyk *et al.* (1996), which decomposed the stress into an elastic component and a viscous (memory) component but did not use different density profiles for elastic and fluid motion. Our approach omits a small magnitude trade-off between compressible elastic deformation and viscous flow that occurs on the order of the Maxwell time (η/μ; about 300 yr for a mantle with 10^{21} Pa s viscosity and 10^{11} Pa shear strength; see above and Cathles 1975). For incompressible mantles, however, this transition does not occur, so no deformation is omitted in separating the elastic and viscous displacements. This separation allows us to address sources of fluid buoyancy independently, as discussed next.

The resulting system of coupled differential equations for the viscous velocities in the transformed radial variable χ is

$$
\frac{\partial}{\partial \chi}
\begin{bmatrix} \dot{h}^V(t) \\ \dot{L}^V(t) \\ f_L(t) \\ F_M(t) \end{bmatrix}
= \hat{\mathbf{A}}^V \cdot
\begin{bmatrix} \dot{h}^V(t) \\ \dot{L}^V(t) \\ f_L(t) \\ F_M(t) \end{bmatrix}
+ \hat{\mathfrak{b}}^V(t), \tag{24}
$$

where the superscript V indicates a viscous component and

$$\hat{\mathbf{A}}^V = \frac{1}{\chi}\frac{2}{2\ell+1}\begin{bmatrix} -\dfrac{2}{\tilde{r}} & \dfrac{(\ell+1)}{\tilde{r}} & 0 & 0 \\[6pt] -\dfrac{\ell}{\tilde{r}} & \dfrac{1}{r} & 0 & \dfrac{2(2\ell+1)}{\tilde{\eta}} \\[6pt] \dfrac{6\tilde{\eta}}{\tilde{r}^2}\dfrac{1}{(2\ell+1)} & -\dfrac{3\tilde{\eta}}{\tilde{r}^2}\dfrac{(\ell+1)}{(2\ell+1)} & 0 & \dfrac{(\ell+1)}{\tilde{r}} \\[6pt] -\dfrac{3\tilde{\eta}}{\tilde{r}^2}\dfrac{\ell}{(2\ell+1)} & \dfrac{\tilde{\eta}}{\tilde{r}^2}\dfrac{(2\ell(\ell+1)-1)}{(2\ell+1)} & \dfrac{\ell}{\tilde{r}} & -\dfrac{3}{\tilde{r}} \end{bmatrix}. \tag{25}$$

The normalization for η and t is the average mantle viscosity $\bar{\eta} = 10^{21}$ Pa s and the time constant for the exponential decay of a harmonic load on a uniform viscous half-space (Cathles 1975):

$$t_{\mathrm{visc}} = \frac{\bar{\eta}(2\ell+1)}{\bar{\rho}g_0 r_E}. \tag{26}$$

Although the matrix $\hat{\mathbf{A}}^E$ (eq. 19) is a 6×6 matrix for two components of displacement, the two components of stress, the potential perturbation and the gravity perturbation, the matrix $\hat{\mathbf{A}}^V$ (eq. 25) is a 4×4 matrix for the viscous velocities and stresses. The gravitational perturbations and stresses from elastic displacements are communicated as source terms to these viscous equations through the vector $\tilde{\mathbf{b}}^V$:

$$\hat{\mathbf{b}}^V(t) = \frac{1}{\chi}\frac{1}{(2\ell+1)^2}\tilde{\rho}\begin{bmatrix} 0 \\ 0 \\ 2\ell+1)q(t) + \left(\tilde{\rho}-\dfrac{4\tilde{g}}{\tilde{r}}\right)h^E(t) + \dfrac{\tilde{g}}{r}(\ell+1)L^E(t) - \tilde{\rho}'_{\mathrm{nonad}}\tilde{g}h^V(t) \\ \dfrac{\tilde{g}}{\tilde{r}}\ell h^E(t) + \dfrac{1}{\tilde{r}}\ell k_d(t) \end{bmatrix}. \tag{27}$$

$\hat{\mathbf{b}}^V$ makes eq. (24) inhomogeneous and makes the flow dependent on the elastic and viscous displacements and gravity perturbations. Most importantly, $\hat{\mathbf{b}}^V$ contains a buoyancy term from the viscous displacement of non-adiabatic density gradients through the term $\tilde{\rho}'_{\mathrm{nonad}}\tilde{g}h^V(t)$ (see eq. 10). Again, the non-adiabatic density represents the degree to which displaced fluid does not immediately equilibrate (in density, temperature, composition, etc.) and so generates a buoyancy that inhibits the approach to iostatic equilibrium. Likewise, the gravitational effect of the viscous displacement of non-adiabatic density gradients in the mantle is source terms for the stresses and gravity of the elastic system. These are communicated to the elastic equations with the vector (Cathles 1975)

$$\hat{\mathbf{b}}^E(t) = \frac{1}{\chi}\frac{1}{(2\ell+1)^2}\tilde{\rho}'_{\mathrm{nonad}}h^V(t)\begin{bmatrix} 0 \\ 0 \\ -\tilde{g} \\ 0 \\ 1 \\ -\dfrac{(\ell+1)}{2\ell+1} \end{bmatrix}, \tag{28}$$

which is added to the right-hand side of eq. (18).

The time-dependent boundary conditions for both the elastic and viscous components of the viscoelastic equations at the top of the viscoelastic mantle ($r = r_M$) are

$$\begin{bmatrix} f_L(t) \\ F_M(t) \\ q(t) \end{bmatrix}_{r=r_M} = \begin{bmatrix} -\alpha - \dfrac{\tilde{\rho}}{2\ell+1}h^V(t) \\ 0 \\ -\alpha - \dfrac{1}{2\ell+1}\left(\tilde{\rho}\left(h^E(t)+h^V(t)\right)+(1+\ell)k_d(t)\right) \end{bmatrix}_{r=r_M} \tag{29}$$

and at the core–mantle boundary are

$$\begin{bmatrix} f_L(t) \\ F_M(t) \\ q(t) \end{bmatrix}_{r=r_c} = \frac{1}{2\ell+1}\begin{bmatrix} \tilde{\rho}_c\tilde{g}_c h^E(t) + (\tilde{\rho}_c-\tilde{\rho}_m)\tilde{g}_c h^V(t) + \tilde{\rho}_c k_d(t) \\ 0 \\ \tilde{\rho}_c-\tilde{\rho}_m)(h^E(t)+h^V(t)) + \dfrac{\ell}{\tilde{r}_c}k_d(t) - \dfrac{\ell}{(2\ell+1)^2}\dfrac{(\tilde{\rho}_c-\tilde{\rho}_m)}{\tilde{r}_c}h^V(t) \end{bmatrix}_{r=r_c}. \tag{30}$$

Here, α is a dimensionless value incorporating the effect of the elastic lithosphere as described next.

The time-domain integration of the viscous velocities is an initial-value differential equation starting with zero-displacement and ending in isostatic equilibrium. At each time t_i, the Ordinary Differential Equation (ODE) in eq. (18) for the instantaneous elastic displacements at t_i is prepared with the inhomogeneity $\tilde{\mathbf{b}}^E$ of eq. (28), using the previously computed viscous displacements ($h^V(t_{i-1})$). These equations are solved using the relaxation method (Press 2007; section 18.3), taking the solutions from t_{i-1} as the initial guess. The inhomogeneity vector for the viscous ODE, $\tilde{\mathbf{b}}^V$ of eq. (27), is prepared using the previously computed viscous displacements ($h^V(t_{i-1})$) and the just computed elastic values. The ODE of eq. (25) is then solved for the viscous velocities at t_i, again using the relaxation method. The viscous displacements for

the next time step t_{i+1} are updated using a fifth-order Dormand–Prince method (a Runge–Kutta method with adaptive step sizes; Press 2007; section 17.2). The equations are stepped forward in time until either equilibrium, when f_L in eq. (29) is below some threshold (e.g. 10^{-6} in dimensionless units), or a prescribed amount of time has elapsed (e.g. the 10^3 ka limit used here).

2.3 The lithosphere

The usual approach to the lithosphere is to treat it as an additional viscoelastic layer with a numerically infinite viscosity (typically around 10^{40} Pa s). A viscosity this large makes the matrix in eq. (25) poorly behaved, so numerical round-off errors compound and lead to unphysical results (Press 2007). Following Cathles (1975) (note the definition of α here is α^{-1} in Cathles 1975), we model the effective elastic lithosphere as an infinitesimally thin shell. Small wavelength loads are supported by elastic stresses in the lithosphere and, therefore, induce less viscoelastic flow in the mantle. The ratio between an applied harmonic stress at the top of the lithosphere and the stress at its bottom that induces the viscoelastic flow in the mantle is

$$\alpha^{-1} = 1 + \frac{(2\ell+1)^4 D}{16 r_E^4 \rho g}, \tag{31}$$

where ρ and g are the density and the gravity of the uppermost part of the viscoelastic mantle and D is the flexural rigidity of the elastic lithosphere, given by

$$D = \frac{1}{3} \frac{\mu(\lambda+\mu)}{\lambda+2\mu} H^3 \tag{32}$$

for a lithosphere with thickness H and Lamé Parameters λ and μ. The limits are $\alpha \to 1$ for $\ell \sim 1$ and $\alpha \to 0$ for $\ell \gg 1$, as expected for a low-pass filter. The lithosphere flexure modifies the viscous velocities by multiplying them by α^{-1}, as noted by McConnell (1965) and Cathles (1975).

Because of the lithospheric support, the mantle can only respond viscoelastically to a portion α of the applied load (again, $0 < \alpha < 1$), hence the $-\alpha$ in the surface boundary conditions used to compute both viscous and elastic components of the viscoelastic flow (eq. 29) as opposed to the -1 in eq. (16) for the elastic response alone. Furthermore, the viscoelastic mantle begins beneath the purely elastic lithosphere (e.g. at a radius r_M, which is at 80 km depth in PREM), and thus the two surfaces do not coincide. Perturbations of the surface of the mantle to the filtered load are thus assumed to transmit to the surface of the lithosphere [see Supporting Information Figs A1(a and b)]. We emphasize the different boundary conditions (filtered load) and domain (core–mantle boundary to r_M) by writing the time-dependent viscoelastic response as $h_{r_M,\alpha}^{\mathrm{VE}}(t)$.

Having computed the response of the viscoelastic mantle, we need to add in the response of the lithosphere for the full response of the surface. Being purely elastic, the response of the lithosphere is immediate and constant in time. The elastic response of the lithosphere that supports the fraction $(1-\alpha)$ of the load, h_{Lith}^E, is the difference between the elastic response of the entire Earth $h_{r_E}^E$, computed from the core–mantle boundary to the surface, and the initial elastic response of the viscoelastic mantle to the filtered load $h_{r_M,\alpha}^E$, computed from the core–mantle boundary to the top of the mantle. We add this response to the time-dependent viscoelastic Love number for the filtered load to obtain the total viscoelastic Love number $h(t)$:

$$h(t) = h_{r_M,\alpha}^{\mathrm{VE}}(t) + h_{\mathrm{Lith}}^E \tag{33}$$

[illustrated in Supporting Information Figs A1 (c and d)]. This correction is also applied to the other Love numbers. For long-wavelength loads (small ℓ), $\alpha \approx 1$ and the total response are dominated by the full viscoelastic relaxation of the fluid mantle. For short-wavelength loads (large ℓ), α approaches zero and the total response is dominated by the purely elastic component, which occurs primarily in the lithosphere. The equispaced mesh in the transformed radial variable χ (eq. 17) concentrates nodes near the surface for higher ℓ (see Supporting Information Fig A3), so we capture small radial variations in elastic parameters near the surface, as in the models VSS96 (Vermeersen *et al.* 1996a; Spada *et al.* 2011) and PREM (Dziewonski & Anderson 1981).

3 RESULTS

3.1 Benchmark of elastic Love numbers

We compute the elastic Love numbers for several models of the Earth's elastic parameters ($\rho(r)$, $\lambda(r)$, $\mu(r)$) of increasing complexity. The first two models are M3-L70-V01 and VSS96 from the viscoelastic benchmarking exercise of Spada *et al.* (2011), which will be used again in the next section to benchmark the time-domain viscoelastic Love numbers. These models are incompressible, with step-wise constant layers: the first has three layers and the second has 28. Their parameters are listed in Tables A1 and A2. The third model is the compressible model 56C-UInc of Pan *et al.* (2015), with 56 step-wise constant mantle layers taken from PREM (Dziewonski & Anderson 1981). The layer parameters are listed in Table A3. The elastic Love numbers for the three models are shown in Fig. 1, computed using the relaxation method on an equally spaced mesh in the transformed radial variable χ of 1000 points, with material parameters linearly interpolated to mesh points. The agreement between the two sets of calculated elastic Love numbers is excellent.
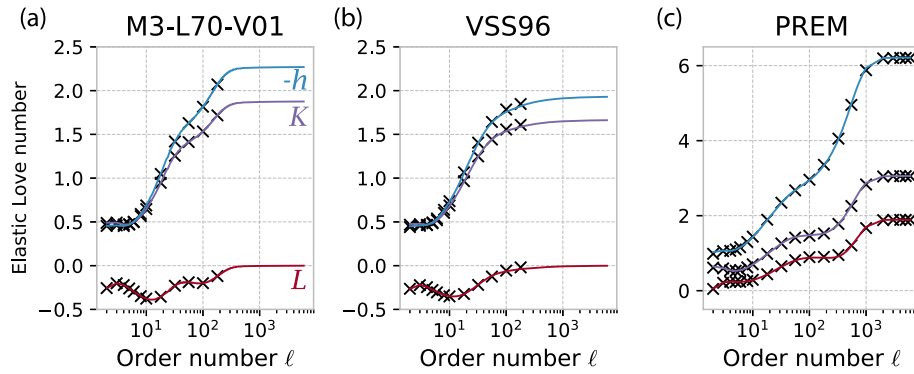
Figure 1. Elastic Love numbers $-h$ (blue), L (red) and K (purple) for $2 \leq \ell \leq 6000$ computed by us using the transformed, normalized relaxation method with 1000 nodes between the core–mantle boundary and the surface (lines) are compared to published Love numbers (the crosses) for (a) M3-L70-V01, (b) VSS96 and (c) PREM. (a) and (b) as reported in Spada *et al.* (2011; which go to $\ell = 256$) and (c) as reported in Pan *et al.* (2015). Note the difference in vertical scales and sign changes between the incompressible (a and b) and compressible (c) deformations.
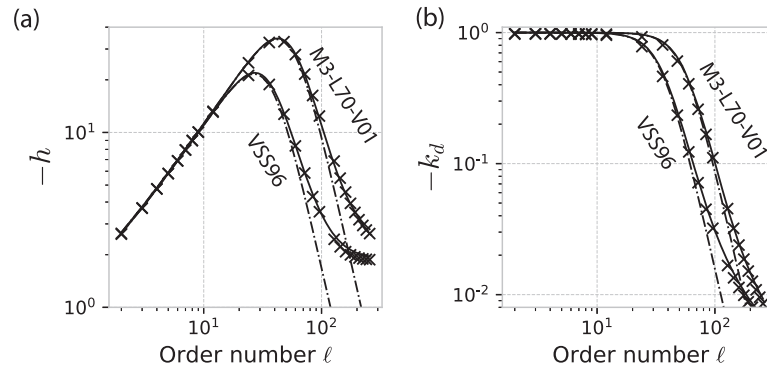
Figure 2. Comparison of viscoelastic Love numbers in the isostatic (equilibrium) limit computed by the method described here (the solid lines) and by the correspondence principle (the crosses) for viscoelastic models M3-L70-V01 and VSS96 from Spada *et al.* (2011). The dash–dotted curves show our Love numbers before the elastic response of the lithosphere has been added back in, for example, when $h = h_\alpha^{\mathrm{VE}}(t)$ rather than $h = h_\alpha^{\mathrm{VE}}(t) + h_{\mathrm{Lith}}^E$.

3.2 Benchmark of viscoelastic Love numbers

We compute the time-domain viscoelastic love numbers using the elastic and viscous profiles of M3-L70-V01 and VSS96 in benchmarking tests 5/1 and 6/1 in Spada *et al.* (2011).
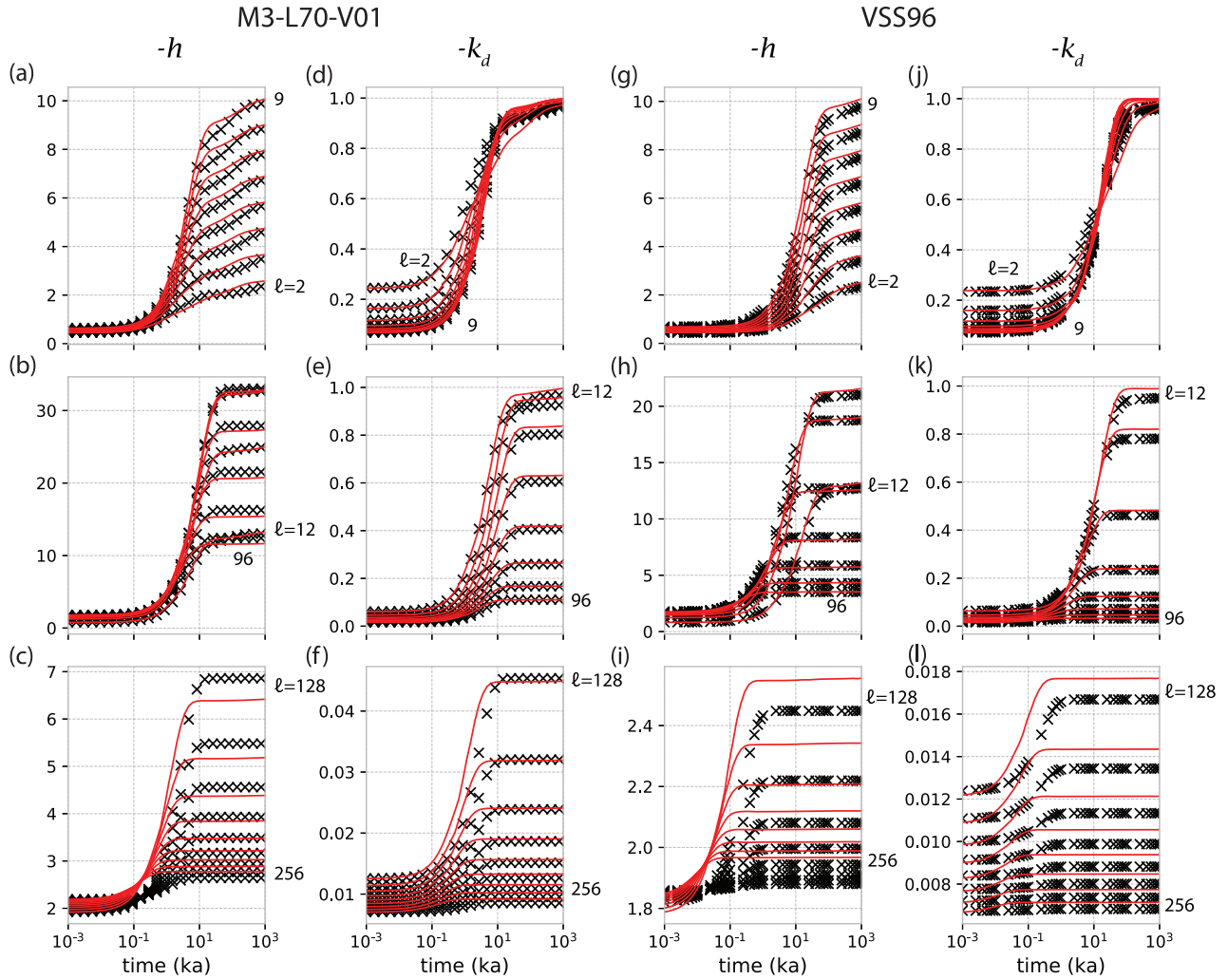
Fig. 2 compares viscoelastic Love numbers in the isostatic (equilibrium) limit. Equilibrium occurs when there are no longer any surface stresses, for example, when $h^V = -\alpha(2\ell + 1)/\tilde{\rho}(r_M)$ (obtained by setting f_L to zero in eq. 29). For long-wavelength ($\ell < 10$) loads, the lithosphere is unimportant and the viscous flow in the mantle isostatically compensates most of the load. For smaller wavelength loads ($\ell \gg 1$), the lithosphere elastically supports more of the load and at short enough wavelengths it supports all of it (where $-h$ becomes constant). The match between the equilibrium Love numbers calculated by our method (the solid line) and the correspondence principle (the crosses) is close, though small differences appear upon closer inspection, as described next. The dash–dotted lines show Love numbers from the original theory of Cathles (1975) for which the elastic response between the surface and the bottom of the lithosphere is not included and thus the Love numbers go to zero for small-wavelength loads.

Fig. 3 compares our time-dependent Love numbers (lines) to those computed by the correspondence principle (the crosses) for an incompressible Earth by Spada *et al.* (2011). The vertical displacement ($-h$, a–c and g–i) and gravity potential perturbation ($-k$, d–f and j–l) Love numbers are shown for two viscoelastic models: M3-L70-V01 (a–f) and VSS96 (g–l). The Love numbers were reconstructed from the M published amplitudes h_i and relaxation times s_i of the normal modes using

$$h(t) = h^E + \sum_{i=1}^{M} h_i(1 - e^{s_i t}), \tag{34}$$

where h^E are the elastic (instantaneous) Love numbers. The other love numbers are reconstructed in a similar fashion (see Vermeersen & Mitrovica 2000; eqs 10–12). The number of modes, M, is determined by the layering of the earth model.

The Love numbers computed by our method agree well with those computed by the correspondence principle for $2 \leq \ell \leq 9$ [Figs 3(a, d, g, j)] and for $12 \leq \ell \leq 96$ (b, e, h, k). For the higher order numbers ($128 \leq \ell \leq 256$) in Figs 3(c, f, i, l), our computed response is faster than that computed using the correspondence principle. The mismatch between the two methods is greater for VSS96 (with a 120 km lithosphere and 28 layers) than for M3-L70-V01 (with a 70 km lithosphere and three layers). Note, however, that the magnitude of the Love numbers is

Figure 3. Viscoelastic load Love numbers calculated by our method (the red lines) compared to those calculated by a correspondence principle method (the black crosses) for models M3-L70-V01 (a–f) and VSS96 (g–l) (Tests 5/1 and 6/1 in Spada *et al.* 2011, respectively) for three sets of order numbers: $2 \leq \ell \leq 9$ (a, d, g, j), $12 \leq \ell \leq 96$ (b, e, h, k) and $128 \leq \ell \leq 256$ (c, f, i, l). The crosses are computed from normal modes reported in Spada *et al.* (2011).

small at high-order numbers (see Fig. 2). Furthermore, when decomposing loads on the scale of the last glacial cycle into spherical harmonics, the power in these order numbers (the C_ℓ^m) is much smaller than the longer wavelength components. Thus, the GIA computed using our Love numbers is not significantly different from the adjustment presented in Spada *et al.* (2011).

This is illustrated in Fig. 4, which compares the GIA resulting from the application of a simple load computed using Love numbers from the two methods for the parameter profiles of M3-L70-V01. The load is a spherical ice cap centred at the north pole, with a radius of $10°$ and a centre height of 1500 m, computed to a maximum order number of $\ell = 128$. This was the load used in benchmark test 1/2 in Spada *et al.* (2011). The load is applied instantaneously at time $t = 0$ and the evolution of the surface is computed at times $t = 1, 2, 5, 10$ ka (thousand years) and the 'equilibrium fluid limit' (10^3 ka, labelled ∞). As seen in the insets, the difference between the models is less than a few percent of the uplift and potential change. For example, the difference in U at 10 ka and colatitude $0°$ is $\sim 6/300 \approx 2$ per cent. The Love number differences between the time-domain and Laplace method of computation, shown in Fig. 3, will not result in uplift or potential differences that are larger than the uncertainty in rebound observations. The changes in potential near $10°$ colatitude at infinite time, and the positive uplift at about $12°$ colatitude at infinite time, reflect the flexure of the 70 km lithosphere under the load. The two computation methods capture this flexure in a similar fashion.

3.3 Benchmark of mantle compressibility and adiabaticity

The effects of compressibility on the viscoelastic deformation are shown in Fig. 5(a) for the PREM elastic parameters, a constant, 10^{21} Pa s mantle and a 70 km lithosphere. Just as reported by Vermeersen *et al.* (1996b) and in fig. 2.9 of Sabadini *et al.* (2016), compressibility increases the magnitude of the elastic (short-time) response to loading, but has no effect on the fluid limit and has little effect on the timing of deformation. Mantle adiabaticity has a much larger effect on the temporal form of the viscoelastic relaxation.
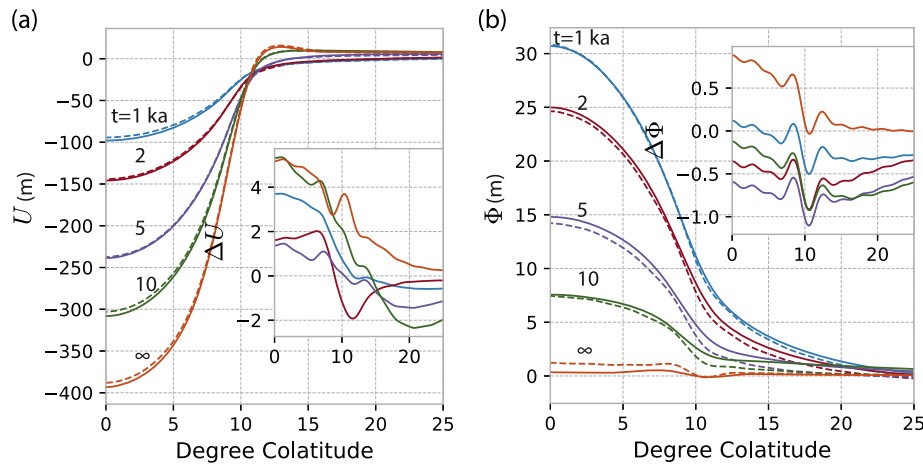
Figure 4. The change in the (a) radial distance to the centre of the Earth, U, and (b) geoid height, Ψ, after the sudden imposition of a $10°$ radius spherical ice cap at the north pole. This corresponds to test 1/2 in Spada *et al.* (2011). The viscoelastic Love used to compute these changes that were computed for earth model M3-L70-V01 with the normalized, transformed relaxation method presented here are shown as the solid lines. The changes computed using Love numbers computed by the correspondence principle methods in TABOO (Spada 2003) are shown as the dashed lines. The curves are shown at 1, 2, 5, 10 and 1000 (labelled ∞) thousand years (ka). The differences between our calculations and the correspondence principle solution are plotted in the inserts.
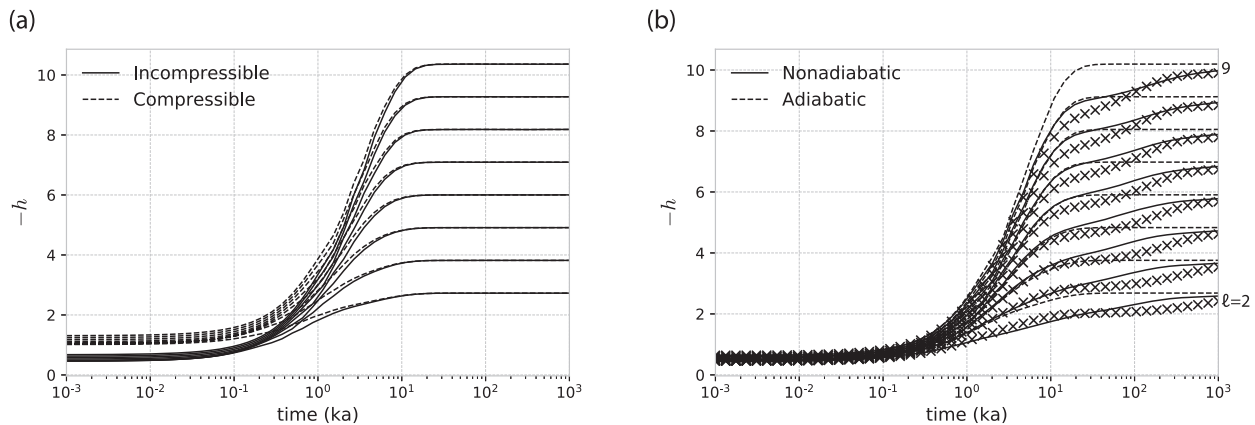

Figure 5. Comparison of viscoelastic Love numbers incorporating (a) compressibility and (b) adiabaticity. (a) Viscoelastic Love numbers for parameter profile PREM with a constant 10^{21} Pa s mantle and a lithosphere with effective elastic thickness of 70 km both compressible (dotted) and incompressible (solid). Compressibility changes the initial elastic deformation but not the equilibrium fluid behaviour. (b) Viscoelastic Love numbers for parameter profile M3-L70-V01 with a fully non-adiabatic mantle $\rho'_{\text{nonad}} = \rho'$ (the solid lines) and a fully adiabatic mantle $\rho'_{\text{nonad}} = 0$ (dashed). The correspondence principle solution of Spada *et al.* (2011) for a fully non-adiabatic mantle is shown in the crosses.

The viscoelastic Love numbers shown in Fig. 3 were computed with an entirely non-adiabatic density gradient (i.e. $\tilde{\rho}'_{\text{nonad}}(r) = \tilde{\rho}'(r)$). Fig. 5(b) shows the viscoelastic response when there are no non-adiabatic density gradients ($\tilde{\rho}'_{\text{nonad}}(r) = 0$) and so the mantle is adiabatic. Without the internal sources of buoyancy, the mantle reaches equilibrium much faster and does not go through the temporal undulations associated with relaxation of the modes of the density stratification.

Fig. 6(a) compares the effect of adiabaticity on the $\ell = 2$ viscoelastic Love number h_2 computed by Nakada (1999; the crosses) to Love numbers computed by our method (lines) for three models with varying degrees of non-adiabaticity: (D0,V0,0), (D1,V0,0) and (D2,V0,0). These correspond to a fully adiabatic mantle (with all density discontinuities removed, D0), a mantle with a non-adiabatic 400 kg m^{-3} density jump at 670 km depth (D1), and a mantle with a constant non-adiabatic gradient in the upper 670 km of the mantle that integrates to 400 kg m^{-3} (D2), respectively. All have a uniform 10^{21} Pa s viscosity mantle (V0) and no lithosphere (0). We were able to reproduce the Love numbers from these models reasonably well (left), but were required to halve the magnitude of the non-adiabatic component of the jump (see Fig. 6b) to do so, a discrepancy that will be explored in future work.

Fig. 6(b) compares the Love numbers of Nakada's (D1, V0, 0) model with a 400 kg m^{-3} density jump at 670 km depth to those computed for an earth model with a density jump at 670 km whose non-adiabatic magnitude is varied between $\Delta\rho_{\text{NA}} = 0$ kg m^{-3} (i.e. adiabatic) and 600 kg m^{-3}. Our continuous method requires spreading the $\Delta\rho_{\text{NA}}$ jump slightly so that there is a constant density gradient over a short range, centred on the discontinuity. We use a 50 km transition—for example, the non-adiabatic density gradient is non-zero 25 km above and below the discontinuity—though the Love numbers computed are not changed by choosing to spread the jump over 25 or 100 km instead. The solid curves show the h_2 Love numbers computed by the time-domain method for a range of non-adiabatic density jumps at 670 km depth. The
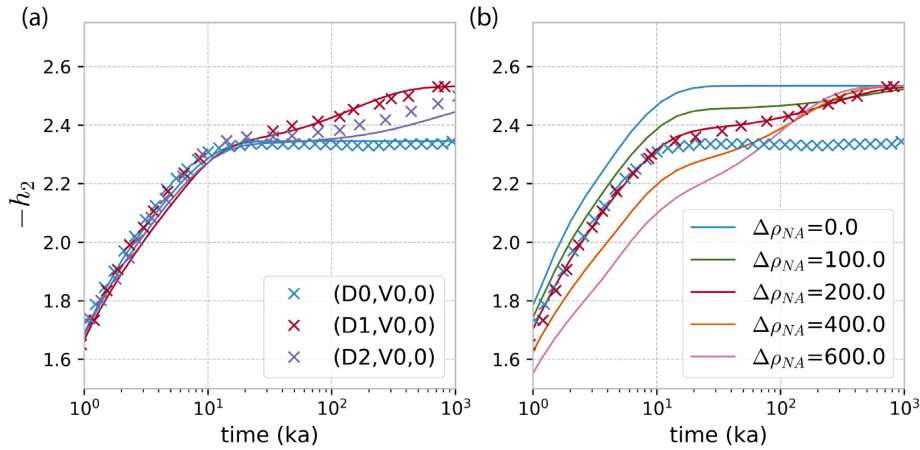
Figure 6. Comparison of our calculated h_2 Love numbers (lines) to those computed by Nakada (1999) for an adiabatic model mantle and model mantles with phase changes as defined in the text. (a) Comparison of three models with different non-adiabatic properties. (b) Comparison of Love numbers from Nakada (1999) for an adiabatic mantle (the blue crosses) and for a mantle with an adiabatic density jump of $400\,\mathrm{kg\,m^{-3}}$ at 670 km depth [the red crosses; model(D1,V0,0)] to Love numbers computed by our method (which do not change mantle density) for non-adiabatic density jumps at 670 km that range from 0 to $600\,\mathrm{kg\,m^{-3}}$.

density profile is not changed. Our adiabatic mantle Love numbers (the blue curve; $\Delta\rho_{NA} = 0$) reaches the same fluid equilibrium value as the Love numbers with non-adiabatic density changes at 670 km. In contrast, the adiabatic model (D0, V0, 0) of Nakada (1999; the blue crosses) modifies the Earth's density to simulate adiabaticity and does not have the same isostatic limit as his model with a $400\,\mathrm{kg\,m^{-3}}$ density jump (D1, V0, 0; the red crosses).

4 DISCUSSION

The benchmarking in the previous section demonstrates that the viscoelastic Love numbers for a fully non-adiabatic mantle computed using the correspondence principle are captured well by our time-domain method. The match is close enough that the computed response to glacial loading are much smaller than the uncertainties in the Earth's observed response (Fig. 4). The differences in the viscoelastic Love numbers revealed by the benchmarking are nevertheless important to understanding these methods of computation, and we discuss these differences in this section.

From Fig. 3, it can be seen that the uplift Love numbers ($-h$) calculated by our time-domain method for the three layer M3-L70-V01 mantle have more pronounced undulations for order numbers 2–9, and fall below the correspondence principle Love numbers at order number 128 before returning to a good magnitude match at still higher order numbers, when the response is mostly elastic. Our potential Love numbers ($-k_d$) agree well in form at all order numbers, lag the correspondence Love numbers slightly at low order numbers (2–9), lead them slightly at high order numbers (128–256) and achieve a greater degree of isostatic compensation ($-k_d = 1$ represents a fully compensated load) at long times. For the 28 layer VSS96 model, our time-domain Love numbers for both uplift and potential lead the correspondence Love numbers and have greater magnitude, most dramatically at order numbers above 128. The time-domain Love numbers again more closely experience more isostatic compensation in the long-time, fluid limit.

The difference in the equilibrium displacements and potential and in the timing are significant, particularly in the amount of load compensation at equilibrium. A load is fully compensated if the gravity perturbation is zero (the gravity of the material displaced balances exactly the gravity of the imposed load; $k_d = -1$). The finite strength of the lithosphere supports some of the load, preventing full compensation of the load, even in isostatic equilibrium. As shown in Fig. 4(b), the potential in the centre of the ice load remains 1.2 m above full compensation 1 million years after the load application in the correspondence principle calculation, but only 0.4 m in the time-domain calculation, a difference of 0.8 m (see inset in Fig. 4b). This difference reduces to 0.6 m if the correspondence principle simulation is taken to 1 billion years. The last stages of relaxation of the low order numbers computed by the correspondence principle method are clearly very slow and exhibit more elastic support. This is also indicated by the slower approach to equilibrium of the crosses in Figs 3(d, g and j).

The differences between the two methods of computation are earth model dependent. For example, the surface uplift Love number computed by the correspondence principle is above our time-domain calculation at large order number for the M3-L70-V01 earth model, but below it for the VSS96 earth model. General features in both models are that the time-domain method computes viscoelastic Love numbers that reach isostatic equilibrium more quickly and completely, and that this feature is more pronounced at high order numbers.

The differences between our Love numbers, computed with an elastic lithosphere and Love numbers calculated using a viscoelastic lithosphere with very high viscosity suggest that the cause of the differences noted above may be the manner in which the two methods treat buoyancy in the lithosphere. The viscoelastic correspondence principle method ascribes buoyancy to any deflection of the top surface of the lithosphere, whereas the elastic lithosphere in the time-domain calculations ascribes buoyancy only at the base of the lithosphere/top of the

viscoelastic mantle. We will investigate the consequences of alternate specifications of the lithosphere in a separate paper, our purpose here being to benchmark our method of Love number calculation against other methods.

5 CONCLUSIONS

This paper fully describes an updated form of the time-domain methods Cathles (1975) used to compute the response of a self-gravitating viscoelastic Earth to surface load redistributions. This method discards the solid-elastic/fluid-elastic transition, which is too small to be of practical consequence in GIA studies, and it specifies the lithosphere as an infinitesimally thin elastic shell as opposed to a viscoelastic layer. Comparing the Love numbers computed using this time-domain method to those computed by the correspondence principle methods for fully non-adiabatic mantles in tests 5/1 and 6/1 of Spada *et al.* (2011), we find good agreement. The two methods produce viscoelastic Love numbers that are similar enough that their application to calculating glacial rebound would produce differences indistinguishable from the noise in current observations.

The most important attribute of our time-domain method is its ability to compute Love numbers that capture varying degrees of adiabaticity in the mantle without modifying the Earth's density profile. The method accomplishes this because the separation of the viscous and elastic equations of motion allows the introduction of a non-adiabatic density profile, the only component of density relevant to flow, that can be varied independently of the density profile. We show that the viscoelastic Love numbers computed by Nakada (1999) for different density jumps across the phase change at 670 km depth can be replicated without modifying the density depth profile.

The method is available for use in the open-source `giapy` (GIA in PYthon) package.

ACKNOWLEDGEMENTS

REFERENCES

Al-Attar, D., 2011. Theoretical problems in global seismology and geodynamics, *PhD thesis,* Oxford University.

Cambiotti, G. & Sabadini, R., 2010. The compressional and compositional stratifications in Maxwell earth models: the gravitational overturning and the long-period tangential flux, *Geophys. J. Int.,* **180**(2), 475–500.

Cathles, L.M., 1971. The viscosity of the earth's mantle, *PhD thesis,* Princeton University.

Cathles, L.M., 1975. *The Viscosity of the Earth's Mantle,* Princeton University Press.

Dziewonski, A.M. & Anderson, D.L., 1981. Preliminary reference earth model, *Phys. Earth planet. Inter.,* **25**(4), 297–356.

Fang, M. & Hager, B.H., 1995. The singularity mystery associated with a radially continuous Maxwell viscoelastic structure, *Geophys. J. Int.,* **123**(3), 849–865.

Farrell, W.E., 1972. Deformation of the Earth by surface loads, *Rev. Geophys. Space Phys.,* **10**(3), 761–797.

Fjeldskaar, W. & Cathles, L., 1984. Measurement requirements for glacial uplift detection of non-adiabatic density gradients in the mantle, *J. geophys. Res.,* **89,** 10 115–10 124.

Han, D. & Wahr, J., 1995. The viscoelastic relaxation of a realistically stratified Earth, and a further analysis of postglacial rebound, *Geophys. J. Int.,* **120,** 287–311.

Hanyk, L., Yuen, D.A. & Matyska, C., 1996. Initial-value and modal approaches for transient viscoelastic responses with complex viscosity profiles, *Geophys. J. Int.,* **127**(2), 348–362.

Johnston, P., Lambeck, K. & Wolf, D., 1997. Material versus isobaric boundaries in the Earth and their influence on postglacial rebound, *Geophys. J. Int.,* **129,** 252–268.

Klemann, V., Wu, P. & Wolf, D., 2003. Compressible viscoelasticity: stability of solutions for homogeneous plane-earth models, *Geophys. J. Int.,* **153,** 569–585.

Martinec, Z., 2000. Spectral-finite element approach to three-dimensional viscoelastic relaxation in a spherical Earth, *Geophys. J. Int.,* **142**(1), 117–141.

Martinec, Z. *et al.*, 2018. A benchmark study of numerical implementations of the sea-level equation in GIA modelling, *Geophys. J. Int.,* **215**(1).

McConnell, R.K., Jr., 1965. Isostatic adjustment in a layered Earth, *J. geophys. Res.,* **70**(20), 5171–5188.

Nakada, M., 1999. Implications of a non-adiabatic density gradient for the Earth's viscoelastic response to surface loading, *Geophys. J. Int.,* **137,** 663–674.

Pan, E., Chen, J.Y., Bevis, M., Bordoni, A., Barletta, V.R. & Molavi Tabrizi, A., 2015. An analytical solution for the elastic response to surface loads imposed on a layered, transversely isotropic and self-gravitating Earth, *Geophys. J. Int.,* **203**(3), 2150–2181.

Peltier, W.R., 1974. The impulse response of a Maxwell Earth, *Rev. Geophys.,* **12,** doi:10.1029/RG012i004p00649.

Peltier, W.R., 1982. Dynamics of the ice age Earth, in *Advances in Geophysics,* pp. 1–146, **24,** ed. Saltzman, B., Academic Press.

Peltier, W.R., 1985. The LAGEOS constraint on deep mantle viscosity: results from a new normal mode method for the inversion of viscoelastic relaxation spectra, *J. geophys. Res.,* **90**(B11), 9411.

Peltier, W.R., Argus, D.F. & Drummond, R., 2015. Space geodesy constrains ice age terminal deglaciation: the global ICE-6G_C (VM5a) model, *J. geophys. Res.,* **120**(1), 450–487.

Press, W.H., 2007. *Numerical Recipes: The Art of Scientific Computing,* 3rd edn, Cambridge Univ. press.

Sabadini, R., Yuen, D.A. & Boschi, E., 1982. Polar wandering and the forced responses of a rotating, multilayered, viscoelastic planet, *J. geophys. Res.,* **87**(B4), 2885.

Sabadini, R., Vermeersen, B. & Cambiotti, G., 2016. *Global Dynamics of the Earth: Applications of Viscoelastic Relaxation Theory to Solid-Earth and Planetary Geophysics,* 2nd edn, Springer.

Spada, G., 2003. The theory behind TABOO, *Samizdat, Golden, Colo.*

Spada, G. & Boschi, L., 2006. Using the post-Widder formula to compute the Earth's viscoelastic love numbers, *Geophys. J. Int.,* **166**(1), 309–321.

Spada, G. *et al.*, 2011. A benchmark study for glacial isostatic adjustment codes, *Geophys. J. Int.,* **185**(1), 106–132.

Steffen, H. & Wu, P., 2011. Glacial isostatic adjustment in Fennoscandia—a review of data and modeling, *J. Geodyn.,* **52**(3-4), 169–204.

Tanaka, Y., Okuno, J. & Okubo, S., 2006. A new method for the computation of global viscoelastic post-seismic deformation in a realistic earth model

(I)—vertical displacement and gravity variation, *Geophys. J. Int.,* **164,** 273–289.

Tromp, J. & Mitrovica, J.X., 1999. Surface loading of a viscoelastic earth—I. General theory, *Geophys. J. R. astr. Soc.,* **137**(3), 847–855.

Turner, J.S., 1979. Buoyancy effects in fluids, in *Cambridge Monographs on Mechanics,* Cambridge Univ. Press.

Vermeersen, L.L.A. & Mitrovica, J.X., 2000. Gravitational stability of spherical self-gravitating relaxation models, *Geophys. J. Int.,* **142**(2), 351–360.

Vermeersen, L.L.A., Sabadini, R. & Spada, G., 1996a. Analytical viscoelastic relaxation models, *Geophys. Res. Lett.,* **23**(7), 697–700.

Vermeersen, L.L.A., Sabadini, R. & Spada, G., 1996b. Compressible rotational deformation, *Geophys. J. Int.,* **126,** 735–761.

Wolf, D., 1985. The normal modes of a uniform, compressible Maxwell half-space, *J. Geophys.,* **56,** 100–105.

Wolf, D., 1991. Viscoelastodynamics of a stratified, compressible planet: incremental field equations and longtime asymptotes, *Geophys. J. Int.,* **104**(2), 401–417.

Wolf, D. & Kaufmann, G., 2000. Effects due to compressional and compositional density stratification on load-induced Maxwell viscoelastic perturbations, *Geophys. J. Int.,* **140**(1), 51–62.

Wu, P. & Peltier, W.R., 1982. Viscous gravitational relaxation, *Geophys. J. R. astr. Soc.,* **70**(2), 435–485.

SUPPORTING INFORMATION

Supplementary data are available at *GJI* online.

ggz276_supporting.pdf

Please note: Oxford University Press is not responsible for the content or functionality of any supporting materials supplied by the authors. Any queries (other than missing material) should be directed to the corresponding author for the paper.